A BL Lacertae object at a cosmic age of 800 Myr

Ekaterina Koptelova (koptelova@astro.ncu.edu.tw)
National Central University
Chorng-Yuan Hwang
National Central University

Letter

Keywords: BL Lacertae objects (BL Lacs), galaxy formation, cosmic age

Posted Date: July 12th, 2021

DOI: https://doi.org/10.21203/rs.3.rs-689340/v1

A BL Lacertae object at a cosmic age of 800 Myr

Ekaterina Koptelova[1]*, Chorng-Yuan Hwang[1]*

[1]*National Central University, Graduate Institute of Astronomy, Taoyuan City, 32001, Taiwan*

BL Lacertae objects (BL Lacs) and flat-spectrum radio quasars (FSRQs), known as blazars, are low- and high-luminosity radio-loud Active Galactic Nuclei (AGNs) with relativistic jets pointed towards Earth[1]. Evolving from FSRQs[2,3], BL Lac objects host $\sim 10^9 M_\odot$ supermassive black holes (SMBHs, where $M_\odot$ is the mass of the Sun) and reside preferentially in giant elliptical galaxies of stellar masses $10^{11} - 10^{12} M_\odot$[4–7]. The known BL Lacs are relatively nearby objects found below redshift 3.6 [3,8,9]. Here, we report the discovery of a BL Lac object, FIRST J233153.20+112952.11 (hereafter J2331+11), at a redshift of 6.57 corresponding to an age of the Universe of ~ 800 Myr. As the typical BL Lac, J2331+11 is a compact radio source with the flat power-law radio continuum, no emission lines in its near-infrared spectrum, and significant variability. The optical-to-radio continuum of J2331+11 is entirely dominated by the synchrotron emission of a relativistic jet. J2331+11 provides evidence for the shorter formation timescale of massive SMBHs with jets and bulge-dominated galaxies than that expected from the Eddington-limited growth of SMBHs and hierarchical galaxy formation. The rapid formation of BL Lacs at early cosmic epochs should have taken place in the densest regions of the early Universe.

The luminous relativistic jets of radio-loud AGNs, including those of blazars, are usually attributed to their more massive SBMHs and correspondingly more massive host galaxies com-

pared to those of radio-quiet AGNs [6,10,11]. The intrinsic luminosities of blazars jets exceed the luminosities of accretion discs around SMBHs [12,13]. Additionally, the jet emission of blazars is relativistically boosted by hundreds of times (a factor of δ^4, where δ is the Doppler factor of the jet [12]). According to the unified scheme of radio-loud AGNs[1], every single blazar implies a parent population of $N_{\rm parent} = 2\Gamma^2$ co-existing objects of similar SMBH masses but randomly oriented jets (where Γ is the bulk Lorentz factor of the jet; for blazars, $\Gamma \approx \delta$ and is typically in a range of $6 - 12$ [3]). Hence, BL Lac objects and FSRQs provide a unique tool to study the spatial distribution of the largest SMBHs up to early cosmic times[14–16].

The progenitors of BL Lac objects, luminous FSRQs, have been discovered up to a redshift of $z \sim 6$ [16–18] implying that billion solar-mass SMBHs can efficiently form on timescales of less than 1 Gyr, constrained by the age of the Universe at $z \sim 6$ [6,19,20]. Moreover, the number density of luminous FSRQs harbouring the largest SMBHs on the order of $\sim 10^9 M_\odot$ was found to be nearly flat up to a redshift of $z \sim 4$ [14]. These luminous FSRQs tentatively suggest that a fraction of them could have evolved into BL Lac objects at the greater redshifts than those of the known BL Lacs, i.e., at $z > 3.6$ [3,8] (see Extended Data Figure 1). The observational evidence of such high-redshift BL Lac objects would provide a new independent constraint on the growth scenario of the largest SMBHs and evolutionary model of blazars.

J2331+11 was identified by matching $z_{\rm PS1}$-band dropouts from the Panoramic Survey Telescope and Rapid Response System 1 (PS1) with the radio sources detected in the Faint Images of the Radio Sky at Twenty centimeters (FIRST) (see Methods). In addition, J2331+11 had counter-

parts in the near-infrared J (1.25 μm), H (1.63 μm), and K (2.20 μm) bands of the United Kingdom Infrared Telescope (UKIRT) Infrared Deep Sky Survey (UKIDSS) Large Area Survey (LAS), in the mid-infrared $W1$ (3.35 μm) and $W2$ (4.60 μm) bands of the Wide-field Infrared Survey Explorer (WISE), in the 3-GHz Very Large Array Sky Survey (VLASS), 1.4-GHz National Radio Astronomy Observatory (NRAO) Very Large Array Sky Survey (NVSS), and 888-MHz Rapid ASKAP (Australian Square Kilometre Array) Continuum Survey (RACS) (see Extended Data Tables 1 and 2). The new deeper near-infrared images obtained with the UKIRT telescope revealed that J2331+11 is not detected at short wavelengths down to a Z(0.88 μm)-band magnitude of 22.95 AB. The spectral energy distribution (SED) constrained by these detailed multi-wavelength data is consistent with the synchrotron-dominated SED of a blazar (see Figure 1b and Methods). Moreover, similar to the typical blazar, J2331+11 represents a compact, unresolved radio source, which shows a flat radio continuum with a spectral index of $\alpha_{\nu,\mathrm{r}} = 0.01 \pm 0.06$[21] (see Methods). Further classification of J2331+11 was obtained using spectroscopic observations. The calculations presented below, assume a flat cosmology with Hubble constant $H_0 = 70\,\mathrm{km\,s^{-1}\,Mpc^{-1}}$, mass density $\Omega_\mathrm{m} = 0.3$ and vacuum density $\Omega_\Lambda = 0.7$.

The spectrum of J2331+11 was obtained with the Gemini Multi-Object Spectrograph of the Gemini North Telescope (Gemini-N/GNIRS) on September 30 and December 24, 2020 (see Figure 1a). The spectrum represents a continuum without emission lines, which can be approximated with power law $f_\nu^\mathrm{obs} \propto \nu^{-\alpha_{\nu,\mathrm{opt}}}$, where $\alpha_{\nu,\mathrm{opt}} = 1.43 \pm 0.23$ is the spectral index of the detected continuum (see Methods). The derived spectral index is consistent within the uncertainty with the spectral index of the non-thermal synchrotron continuum showing the $f_\nu^\mathrm{S} \propto \nu^{-3/2}$ flux dependence[22]. For

comparison, the thermal emission of the accretion discs of quasars is characterised by a flatter continuum with a spectral index of $\sim$0.44. The continuum shows a break in flux (the Gunn-Peterson trough) at $\sim$0.921 μm due to absorption by neutral hydrogen in the intergalactic medium at high redshifts (see Extended Data Figure 2), which provides the lower limit on the redshift of J2331+11 to be $z \approx 6.57$. The UKIDSS LAS and Gemini-N observations conducted at different epochs separated by approximately ten years revealed significant variability of J2331+11. In the Gemini-N/GNIRS observations, the rest-frame UV/optical continuum of J2331+11 was steeper compared to that during the UKIDSS LAS observations with a spectral index of $\alpha_{\nu,\mathrm{opt}} \approx 0.27$ as estimated from the H- and K-band fluxes (see Figure 1a and Methods). The UKIDSS LAS and PS1 photometry in the H and y_{PS1} bands indicate that J2331+11 was more than 0.5 magnitudes brighter during the PS1 and UKIDSS observations in 2011-2014 and 2009 compared to the later observations in 2020 (see Figure 1a and Extended Data Table 1). The radio flux of J2331+11 also showed variations of approximately 15% between the observations by the FIRST survey and the later observations by the RACS and VLASS surveys (see Extended Data Figure 3 and Extended Data Table 2). Hence, J2331+11 satisfy the classical criteria of a BL Lac object[4,8,23]: no or weak emission lines of rest-frame equivalent widths of less than 5Å, detection in the radio or X-ray bands, compact radio morphology, flat radio continuum emission, and significant variability at all wavelengths.

The SEDs of BL Lac objects are produced by the non-thermal synchrotron self-Compton (SSC) emission process within the relativistic jet and show two emission peaks[21,22]: the radio-to-UV/soft X-ray peak due to synchrotron cooling of relativistic electrons in the jet ("synchrotron

peak" in Figure 1b) and the hard X-ray to γ-ray peak due to inverse Compton scattering of synchrotron photons on the electrons. The absence of broad emission lines in the spectra of many BL Lac objects suggests that the contribution of the thermal emission of the accretion disc into the SEDs of BL Lac objects is negligible compared to the non-thermal jet emission [4,21,24]. The observed optical-to-radio SED of J2331+11 is consistent with the synchrotron peak of BL Lacs, e.g., with that of the high-redshift BL Lac object J1219+36 at $z = 3.59$ [9] (see Extended Data Figure 4). The synchrotron peak of J2331+11 is observed close to its maximum, which approximately occurs in the mid-infrared wavelengths and falls into the intermediate-synchrotron peak frequencies, $10^{14} - 10^{15}$ Hz in the rest-frame of J2331+11 [21] (see Figure 1b). The model of the synchrotron SSC process implies that the emission of J2331+11 originates from an emitting region of size $R \approx 2.1 \times 10^{16}$ cm, which is approximately equal to 70 gravitational radii of a $10^9 M_\odot$ SMBH and corresponds to the acceleration and collimation zone of the jets of blazars [23]. The region has the magnetic field of intensity $B \sim 0.4$ G and electrons of density $N \sim 10\,\mathrm{cm}^{-3}$ accelerated up to a Lorentz factor of $\gamma_{\rm peak} \sim 10^3$ (see Extended Data Table 3). The Doppler factor of the region is $\delta \sim 31.5$ producing a total luminosity of the observed synchrotron peak of $L_{\rm S} \approx 2.4 \times 10^{47}\,\mathrm{erg\,s^{-1}}$. This luminosity is comparable to the bolometric luminosities of the accretion discs of luminous high-redshift quasars at $z > 6$ [20]. The rest-frame frequency of the synchrotron peak of J2331+11 from the SSC emission model is 3.8×10^{14} Hz (see Extended Data Table 3).

The radio luminosity of J2331+11 at rest-frame 5 GHz is comparable to those of radio luminous BL Lac objects at low redshifts (see Extended Data Figure 1) and is $L_{\rm 5GHz} = 4\pi D_{\rm L}^2 f_\nu^{\rm obs}(1+z)^{\alpha_{\nu,\rm r}-1} \approx 1.6 \times 10^{33}\,\mathrm{erg\,s^{-1}\,Hz^{-1}}$ (where $D_{\rm L}$ is the luminosity distance, $f_\nu^{\rm obs}$ is the observed

radio flux at 888 MHz, which is close to the frequency of 5 GHz at the rest-frame of J2331+11, $\alpha_{\nu,\mathrm{r}} \approx 0$ is the radio spectral index, and z is the redshift of J2331+11). In the nearby Universe, the number density of such luminous BL Lacs is less than $1\,\mathrm{Gpc}^{-3}$ [4,25]. The 5-GHz radio luminosities and masses of the SMBHs of low-redshift BL Lac objects correlate approximately as $L_{5\mathrm{GHz}} \propto M_{\mathrm{BH}}^{0.6}$, where M_{BH} is the SMBH mass from the stellar velocity dispersion–host galaxy bulge relation[26]. The $L_{5\mathrm{GHz}} \propto M_{\mathrm{BH}}^{0.6}$ relation, derived for the nearby BL Lac objects with average SMBH masses of $2 \times 10^8 M_\odot$, implies that the Doppler amplification of the jet emission is usually higher for more massive SMBHs. Assuming this relation, a factor of $\gtrsim 10$ higher radio luminosity of J2331+11 compared to those of the nearby BL Lacs suggests an SMBH of greater than $9 \times 10^9 M_\odot$. Most of the known luminous high-redshift blazars, mostly FSRQs, harbour SMBHs of comparable masses[13–15].

The evolution of blazars follows the change in the accretion mode of SMBHs [2,3]. The SMBHs of FSRQs grow in gas-rich environments at accretion rates of $L_{\mathrm{bol}}/L_{\mathrm{Edd}} \sim 0.1-1$ (where L_{bol} is the bolometric luminosity of the accretion disc, $L_{\mathrm{Edd}} = 1.26 \times 10^{38} (M_{\mathrm{BH}}/M_\odot)\,\mathrm{erg\,s^{-1}}$ is the Eddington luminosity). The SMBHs of BL Lac objects, on the other hand, have consumed most of their gas during the FSRQ phase and accrete in the regime of radiatively inefficient advection-dominated accretion flows. In this regime, the luminosity of the accretion disc is typically below 1% of the Eddington luminosity [2,5,24]. The observations of blazars indicate that transition from the FSRQs to BL Lac accretion mode occurs approximately at an accretion rate of $L_{\mathrm{bol}}/L_{\mathrm{Edd}} \approx 5 \times 10^{-3}$, at which the bolometric luminosity of the accretion disc drops below $\sim 10^{45}\,\mathrm{erg\,s^{-1}}$, and the non-thermal emission of the jet starts to dominate the thermal emission of

the accretion disc [24]. The mass of the SMBH of J2331+11 estimated assuming that the bolometric luminosity and accretion rate of its accretion disc are equal to those of an object in the transition phase, is $\sim 2 \times 10^9 M_\odot$. Thus, the upper limit on the luminosity of the accretion disc of J2331+11 also suggests a massive SMBH on the order of $10^9 M_\odot$. This mass should have been accumulated at earlier cosmic epochs ($z > 6.57$) since the growth rates of the SMBHs of BL Lac objects are extremely low compared to those of quasars. During the FSRQ phase, the individual episodes of the rapid SMBH growth can be triggered by close galaxy interactions and may last for ~ 0.1 Gyr[27]. If J2331+11 had undergone at least one such episode, then its SMBH should have been already sufficiently massive when the Universe was younger than 700 Myr, corresponding to $z \gtrsim 7.3$. The efficient growth of the SMBH of J2331+11 suggests a high accretion rate of a few times of the Eddington luminosity during the FSRQ phase, comparable to those observed in some high-redshift quasars [20,28].

The host galaxies of low-redshift BL Lac objects are giant elliptical or cD galaxies usually found in the groups or clusters of galaxies [4,5,27]. For example, the nearest BL Lac-prototype radio galaxy M87 is one of the most massive galaxies in the Virgo cluster with an SMBH of $6.6 \times 10^9 \mathrm{M}_\odot$[29]. Moreover, in the nearby Universe, the host galaxies of AGNs of radio luminosities $L_{5\mathrm{GHz}} > 10^{31}\,\mathrm{erg\,s^{-1}\,Hz^{-1}}$ are all massive elliptical galaxies[10]. In the hierarchical scenario of galaxy formation, massive bulge-dominated galaxies assemble at relatively late cosmic epochs through consecutive mergers of individual galaxies[30]. If the host galaxy of J2331+11 is as massive as those of low-redshift BL Lacs, J2331+11 was probably formed in one of the densest regions of the early Universe, in which the SMBHs and bulges of massive galaxies could have assembled

rapidly.

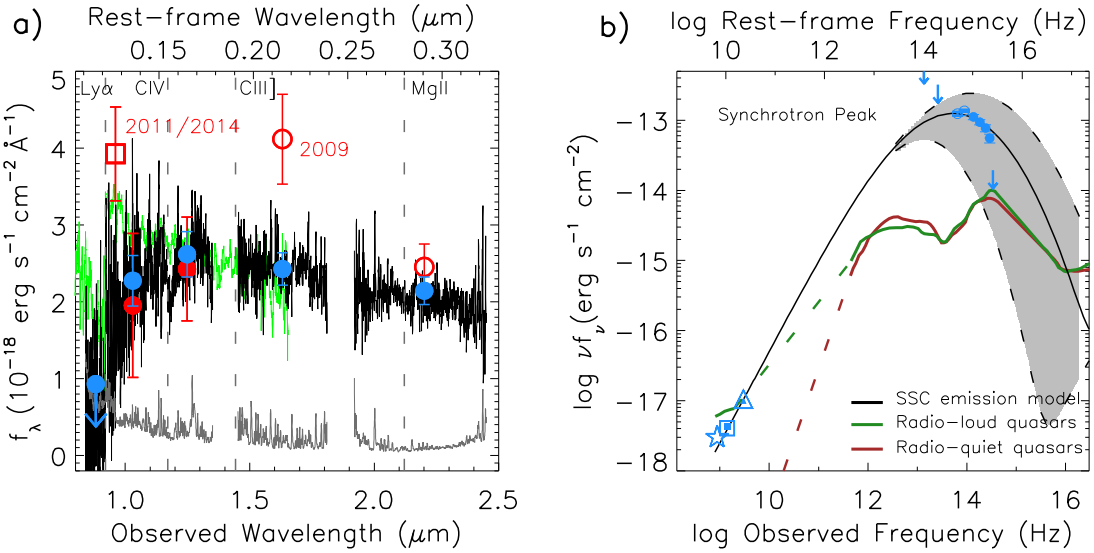

Figure 1: **a) Gemini-N/GNIRS spectrum of J2331+11 (black).** The 1σ error spectrum is shown with a grey line. The fluxes in the Z, Y, J, H, and K bands measured at the epoch close to the Gemini-N/GNIRS observations are shown with blue symbols. The red symbols show the archival fluxes in the PS1 $y_{\rm PS1}$ band (open square), UKIDSS LAS Y and J (filled circles), and H and K bands (open circles) obtained at different epochs. The vertical dashed lines mark the expected wavelengths of prominent broad emission lines of quasars. The redshift-corrected SDSS spectrum of the BL Lac object J1219+36 at $z = 3.59$[9] is overplotted in green for comparison. **b) Optical-to-radio SED of J2331+11.** The SED is constructed using the K-corrected near-infrared Y, J, H, K (filled circles), mid-infrared $W1$ and $W2$ (open circles), and the 3-GHz VLASS (open and filled triangles), 1.4-GHz FIRST (open square), 1.4-GHz NVSS (filled square), and 888-MHz RACS (open star) fluxes. The upper limits on the Z, and mid-infrared $W3$ and $W4$ fluxes are shown with arrows. The synchrotron SSC emission model of the synchrotron peak of J2331+11 is shown with a black line. The shaded region between two dashed lines corresponds to the SEDs of intermediate synchrotron peaked blazars, which peak within rest frequencies $10^{14} - 10^{15}$ Hz. The SEDs of radio-loud and radio-quiet quasars are overplotted for comparison.

Methods

Photometry. J2331+11 was found by matching $z_{\rm PS1}$-band dropouts from the PS1 3π survey[32] multi-epoch stack catalogue with the FIRST catalogue of 1.4-GHz radio sources [33,34]. The PS1 stack catalogue is based on the data taken between 2010 and 2014 and has 5σ AB limiting magnitudes of 23.3, 23.2, 23.1, 22.3, and 21.3 in the $g_{\rm PS1}$, $r_{\rm PS1}$, $i_{\rm PS1}$, $z_{\rm PS1}$, and $y_{\rm PS1}$ bands, respectively. J2331+11 was detected in the $y_{\rm PS1}$-band stack image, but not detected in the bluer bands. The FIRST survey, which has a median sensitivity of 0.141 mJy beam^{-1} and an angular resolution of 5 arcsec, detected J2331+11 at a signal-to-noise ratio of $\sim$14. The PS1 and FIRST positions of J2331+11 matched within 0.4 arcsec. The additional near-, mid-infrared and radio data of J2331+11 were obtained using different observations described below and summarised in Extended Data Tables 1 and 2. The magnitudes in Extended Data Table 1 are given in the AB photometric system.

Near-infrared data. The near-infrared photometric and imaging data of J2331+11 include archival data obtained by the UKIDSS LAS survey[35] conducted with the Wide Field Camera (WFCAM) of the 3.8-m UKIRT telescope in the Y(1.0 μm), J(1.2 μm), H(1.6 μm), and K(2.2 μm) bands in 2009, and new UKIRT WFCAM data in the Z, Y, J, H, and K bands obtained in 2020. The reported UKIDSS LAS H- and K-band magnitudes are from the Data Release 8 (DR8) source catalogue. In the Y and J bands, J2331+11 was detected with a low signal-to-noise ratio of less than 2, and these data were not included in the DR8 catalogue. The Y and J magnitudes provided in Extended Data Table 1 were measured directly from the UKIDSS LAS images. The new deeper UKIRT WFCAM images of J2331+11 were obtained at the epoch close to the spectroscopic obser-

vations with Gemini-N/GNIRS. The images were taken in the nine-point dither sequence with total exposure times of 720, 540, 270, 180, and 180 s in the Z, Y, J, H, and K bands, respectively. The new images were processed with the same photometric pipeline as the previous UKIDSS LAS data [36], which excludes systematic uncertainties in the near-infrared fluxes of J2331+11 from different epochs. The UKIRT Vega magnitudes were transformed into AB magnitudes [36].

Mid-infrared data. The SED of J2331+11 was constructed using the unWISE[37] $W1$ (3.4 μm) and $W2$ (4.6 μm) fluxes measured from data collected by the WISE[38] and NEOWISE[39] missions between 2010 and 2017. The 2σ upper limits on the $W3$ (12 μm) and $W4$ (22 μm) fluxes of J2331+11 are from the AllWISE source catalogue, which is based on the shallower data collected by the WISE mission between 2010 and 2011. The WISE Vega magnitudes were transformed into AB magnitudes.

Radio data. J2331+11 was independently detected at 0.888, 1.4, and 3 GHz by the RACS [40], FIRST[33,34], and VLASS[41] radio surveys, respectively. The most recent data close to the epoch of the Gemini-N/GNIRS spectroscopic observations were obtained in 2020 by the RACS and VLASS surveys. The RACS survey is an all-sky survey south of a declination $\delta = +51$ deg in a frequency range of $700 - 1800$ MHz. The initial data release (December 2020) [40] included sources detected at 888 MHz with a median sensitivity of 0.26 mJy beam^{-1} and an angular resolution of $15 - 25$ arcsec. The synoptic (3-epoch observations separated by 32 months) VLASS survey at 3 GHz[41] has a sensitivity of 0.12 mJy beam^{-1} per epoch and an angular resolution of 2.5 arcsec. J2331+11 was observed by VLASS at two different epochs, during campaigns VLASS1.1 in 2017 and VLASS2.1 in 2020. The integrated flux density of J2331+11 was measured from the VLASS

Quick Look images available from $www.cirada.ca$. J2331+11 is also included in the catalogue of sources detected during the first epoch of the survey, VLASS1.1 Quick Look catalogue available from $www.cirada.ca/catalogues$. The integrated flux density of J2331+11 measured from the VLASS1.1 Quick Look image is consistent with that provided in the VLASS1.1 Quick Look Catalogue.

J2331+11 was marginally detected by the 1.4-GHz NVSS survey [42] with a signal-to-noise ratio of $5-6$. The survey conducted between 1993 and 1996 has a typical sensitivity of approximately 0.45 mJy beam^{-1} and an angular resolution of 45 arcsec. J2331+11 was not included in the NVSS catalogue of the detected sources; the integrated flux density of J2331+11 was measured from the NVSS images. The measured flux is consistent within uncertainties with the integrated flux density provided by the FIRST survey at the same frequency.

Spectroscopic observations. The spectroscopic data of J2331+11 were obtained on September 30 and December 24, 2020, using the Gemini-N/GNIRS spectrograph [43] in cross-dispersed mode (XD) and a slit width of 1 arcsec. The slit was oriented at a fixed position angle of 0 deg to avoid contamination from a brighter source a few arcseconds to the east of J2331+11. The instrument setup provided spectral coverage of $0.85-2.5\,\mu$m, and a resolution of $R\approx 500$. The observations were executed in the standard ABBA dither sequence. The individual exposure times at each dither position were 293 s on September 30 and 265 s on December 24. The total exposure time of the data was 3.75 h. The spectra obtained on different dates were reduced and wavelength calibrated independently using the Gemini IRAF package. The resulting 2D spectra were normalised by the exposure time, rectified onto the same wavelength grid, and stacked. The 1D spectrum of J2331+11

and the error spectrum were obtained from the resulting 2D stack spectrum and its variance. The telluric correction and absolute flux calibration was performed using two standard stars observed before and after J2331+11 at similar airmass: HIP109939 (spectral type A1Vn) and HIP5310 (A3V). The reduction procedure for the stars was similar to that of J2331+11. The telluric lines were removed by dividing the 1D spectrum of J2331+11 by the 1D spectrum of star HIP109939. The flux calibration was performed by multiplying the obtained ratio by the blackbody model spectrum of the star. To verify the quality of the telluric correction and flux calibration, the same procedure was repeated using star HIP5310. Both stars yielded the same spectral flux of J2331+11, uncertain by less than 1%. The final flux calibrated spectrum of J2331+11 agrees with the UKIRT Z, Y, J, H, and K photometric fluxes independently measured at a similar epoch.

UV/Optical and radio spectral indices. Within small spectral intervals, the observed SED of J2331+11 was represented by power law $f_\nu^{\rm obs} \propto \nu^{-\alpha_\nu}$, where α_ν is the spectral index. The radio spectral index ($\alpha_{\nu,\rm r}$) was estimated using the radio fluxes measured by the RACS and VLASS2.1 surveys at 888 MHz and 3 GHz at two quasi-simultaneous epochs separated by approximately two months (see Extended Data Table 2). These quasi-simultaneous fluxes are considered to be less affected by variability of J2331+11. Additionally, the RACS and VLASS2.1 measurements are also quasi-simultaneous with the spectroscopic observations as they were obtained within approximately one and four months of the Gemini-N/GNIRS spectrum. The radio spectral index and spectral index uncertainty were calculated as follows

$$\alpha_{\nu,\mathrm{r}} = -\frac{\ln(\mathrm{f}_{\nu_1}/\mathrm{f}_{\nu_2})}{\ln(\nu_1/\nu_2)}, \tag{1}$$

and

$$\sigma_{\alpha_{\nu,\mathrm{r}}} = \frac{1}{|\ln(\nu_1/\nu_2)|}\sqrt{\left(\frac{\sigma_{f_{\nu_1}}}{f_{\nu_1}}\right)^2 + \left(\frac{\sigma_{f_{\nu_2}}}{f_{\nu_2}}\right)^2}, \tag{2}$$

where $f_{\nu_{1,2}}$ and $\sigma_{f_{\nu_{1,2}}}$ are the flux densities and flux density uncertainties measured at frequencies $\nu_1 = 888\,\mathrm{MHz}$ and $\nu_2 = 3\,\mathrm{GHz}$. The derived spectral index is $\alpha_{\nu,\mathrm{r}} = 0.01 \pm 0.06$ and is consistent with a flat radio continuum of $\alpha_{\nu,\mathrm{r}} \sim 0$ typical for blazars [21]. The power-law fit to all available radio data gives a similar value of $\alpha_{\nu,\mathrm{r}} = 0.00 \pm 0.09$ (see Extended Data Figure 3).

The spectral index of J2331+11 at rest-frame UV/optical wavelengths is $\alpha_{\nu,\mathrm{opt}} \approx 1.42 \pm 0.23$. It was derived from the power-law fit of the Gemini-N/GNIRS spectrum between 1.27 and 2.40 μm (excluding regions of strong atmospheric absorption). The uncertainty on the spectral index was estimated from a sample of artificial spectra simulated from the Gemini-N/GNIRS spectrum by adding a normally distributed flux error at each spectral point.

The observed near-infrared and radio fluxes were K-corrected using the following relation: $f_\nu = f_\nu^{\mathrm{obs}}(1+z)^{\alpha_\nu - 1}$, where f_ν^{obs} is the observed flux density, α_ν is the spectral index measured in the near-infrared or radio wavelengths, and z is the redshift of J2331+11.

SED model. The SED of J2331+11 presented in Figure 1b was constructed using the K-corrected UKIRT Z, Y, J, H, and K fluxes measured in 2020, the $W1$, $W2$ fluxes from the unWISE

catalogue, the upper limits on the $W3$, $W4$ fluxes, and the radio fluxes at 0.888, 1.4 and 3 GHz. It was assumed that these data provide a good representation of the typical SED of J2331+11. Moreover, the near-infrared and radio fluxes at 0.888 and 3 GHz were measured at close epochs separated by only 1-4 months. The SED was modelled using the synchrotron self-Compton (SSC) emission model[44], which is commonly used to describe the double-peak SEDs of BL Lac objects[21]. The model assumes that the observed emission originates from an emitting region moving with the relativistic speed in the jet; the emission is boosted by a Doppler factor of $\delta = 1/[\Gamma(1 - \beta\cos\theta)]$, where $\Gamma = 1/\sqrt{1-\beta^2}$ is the bulk Lorentz factor of the emitting region, β is the velocity in units of the the speed of light, and θ is the angle between the line of sight and jet. The synchrotron SSC emission spectrum of the emitting region is computed assuming that the electrons are isotropically distributed in a homogeneous randomly oriented magnetic field and have the log-parabolic energy distribution of the form [21,45,46]:

$$n(\gamma) = K \times 10^{r(\log(\gamma/\gamma_{\rm peak}))^2}, \tag{3}$$

where K is the normalisation coefficient, $\gamma_{\rm peak}$ is the electron Lorentz factor at the peak of the electron energy distribution, and r is the curvature parameter. Assuming this electron distribution, the model has the following free parameters: intensity of magnetic field B (G), radius of the emitting region R (cm), Doppler boosting factor δ, curvature parameter r, electron Lorentz factor at the peak of the electron energy distribution $\gamma_{\rm peak}$, minimum and maximum Lorentz factors of the electron energy distribution $\gamma_{\rm min}$ and $\gamma_{\rm max}$, and electron density $N = \int_{\gamma_{\rm min}}^{\gamma_{\rm max}} n(\gamma) d\gamma$ (cm^{-3}).

The synchrotron SSC emission model of J2331+11 was calculated for the fixed minimum and maximum energies of the electrons, $\gamma_{\rm min} = 10^{-1}$ and $\gamma_{\rm max} = 10^{6}$, as the change of this parameters has little effect on the resulting model. Additionally, the observed brightness variation of J2331+11 provides a constraint on the size of the emitting region. The UKIDSS LAS photometry of J2331+11 obtained in 2009 suggests that the pairs of fluxes, Y and J, and H and K, measured 61 days apart, may correspond to two different brightness states of J2331+11 (see Figure 1 and Extended Data Table 1). The Y and J fluxes, which are consistent with the fluxes during the recent UKIRT observations in 2020 and with the Gemini-N/GNIRS fluxes, seem to correspond to the typical brightness state of J2331+11. The H and K fluxes, on the other hand, were likely measured during the high brightness state characterized by a bluer $H-K$ color and a flatter rest-frame UV/optical continuum of $\alpha_{\nu,\rm opt} \sim 0.27$. From the timescale of the observed brightness variation ($t_{\rm var}$), the radius of the emitting region is estimated to be $R = ct_{\rm var}/(1+z) \approx 2.1 \times 10^{16}$ cm, where c is the speed of light. The inferred radius is consistent with the typical size of the emitting regions of BL Lacs as derived from their variability timescales, e.g., [47]. The radius of the emitting region was then fixed in the calculation of the synchrotron SSC emission model. The parameter search of the model was performed using the online[1] numerical SSC code[46] by first varying parameters, B, N, and δ, which contribute into the strength of the observed flux, and then by varying r and $\gamma_{\rm peak}$, which determine the shape and peak frequency of the model. The model that best describes the data is shown in Figure 1b; the parameters of the model are summarised in Extended Data Table 3. The luminosity of the synchrotron peak of J2331+11 provided in the table was estimated from the SSC emission model as $L_{\rm S} = 4\pi D_{\rm L} \int f_\nu d\nu$, where $\int f_\nu d\nu$ is the model flux integrated

[1] https://tools.ssdc.asi.it/SED/

between observer-frame frequencies 0.8×10^9 and 4×10^{16} Hz, $D_{\rm L}$ is the luminosity distance. The observed SED is well reproduced by a single SSC emission component suggesting that the contribution from external emission components such as the accretion disc or dust torus is negligible. The synchrotron and inverse Compton peaks of J2331+11 predicted by the SSC emission model are shown in Extended Data Figure 4 in comparison with the SED of the BL Lac object J1219+36 at $z = 3.59$ [9].

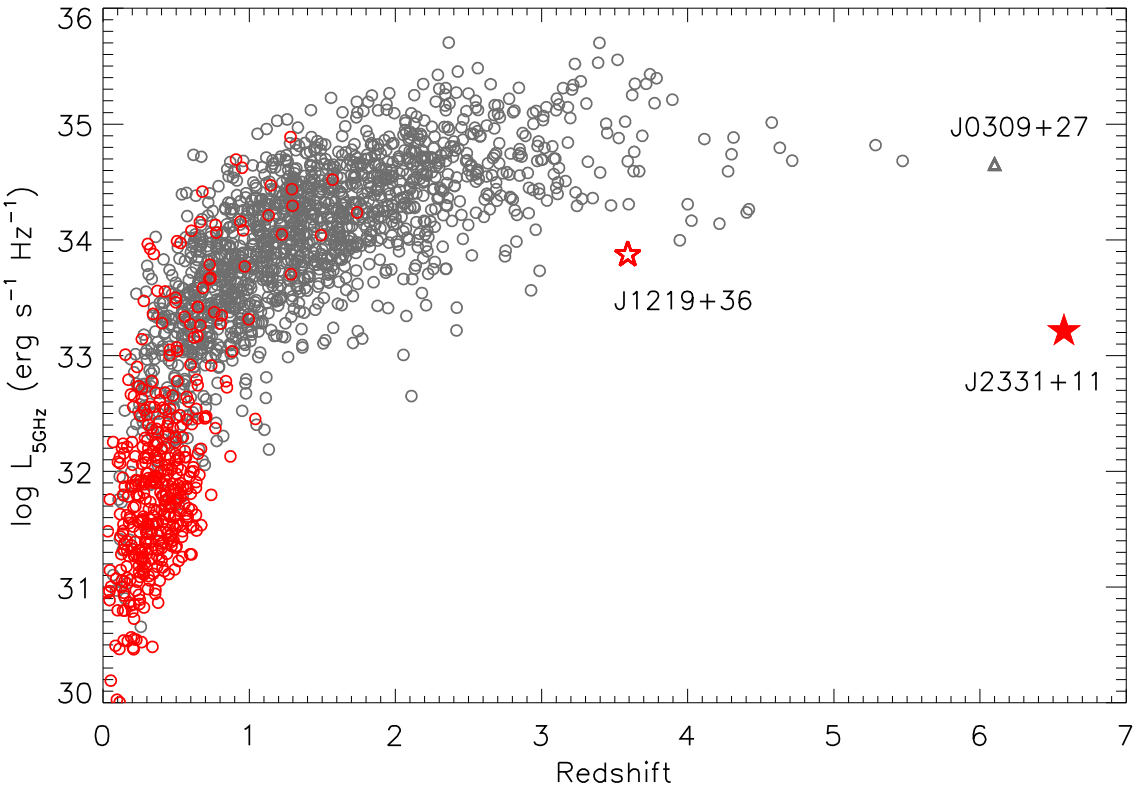

Extended Data Figure 1. Radio luminosity of blazars versus redshift. The black and red open circles depict FSRQs and BL Lac objects from the fifth edition of the ROMA-BZCAT multifrequency catalogue of blazars [31]. J2331+11 is shown with a red filled star. The high-redshift BL Lac object J1219+36 at $z = 3.59$[9] and the most distant FSRQ currently known, J0309+27 at $z = 6.10$[16], are shown with an open star and a triangle, respectively. The radio luminosities at rest-frame 5 GHz ($L_{5\mathrm{GHz}}$) were estimated using the 3-GHz radio fluxes from the VLASS1.1 Quick Look Catalogue assuming a flat radio continuum with a spectral index of $\alpha_{\nu,\mathrm{r}} = 0$. The luminosity of J0309+27 was estimated using the 1.4-GHz radio flux and spectral index from the discovery paper [16].

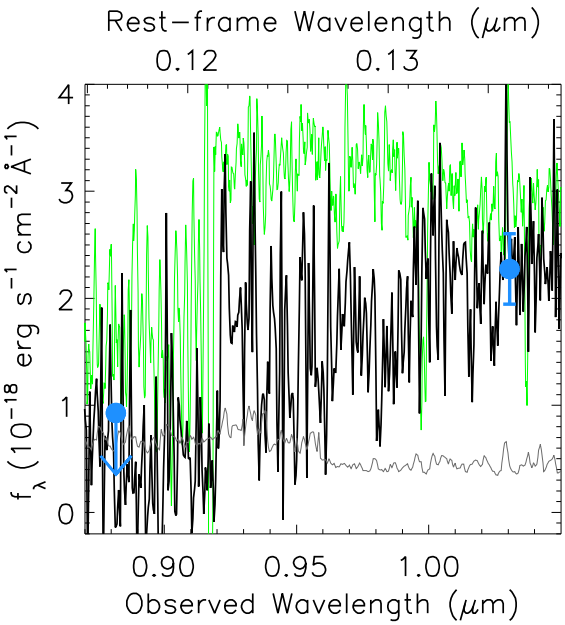

Extended Data Figure 2. Enlarged view of the continuum break at 0.921 μm. The Gemini-N/GNIRS spectrum and 1σ error spectrum of J2331+11 are shown with black and grey lines, respectively. The spectrum is presented at the original GNIRS spectral resolution of $\sim$3 Å per spectral element. The blue symbols correspond to the UKIRT Z-band upper flux limit, and Y-band flux measured quasi-simultaneously with the spectrum. The redshift-corrected SDSS spectrum of the BL Lac object J1219+36 at $z = 3.59$[9] is overplotted in green for comparison.

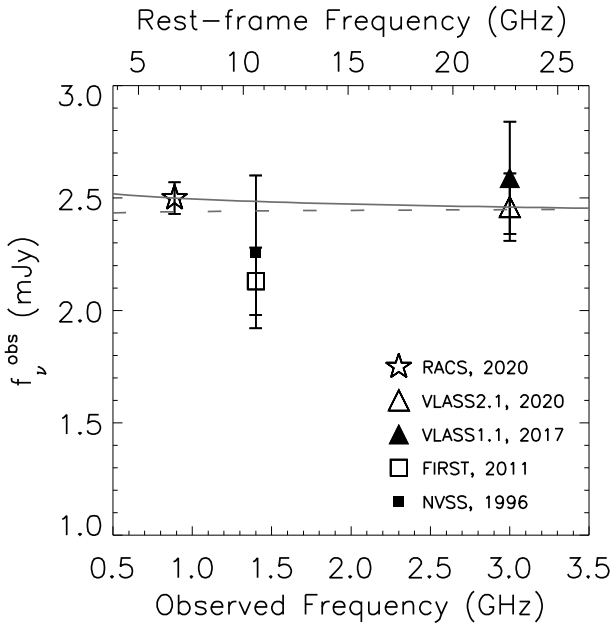

Extended Data Figure 3. Integrated radio flux densities of J2331+11. The different symbols mark flux densities measured with different instruments and at different epochs. The lines correspond to the power laws ($f_\nu^{\rm obs} \propto \nu^{-\alpha_{\nu,\rm r}}$) with a spectral index of $\alpha_{\nu,\rm r} = 0.01 \pm 0.06$ derived from the quasi-simultaneous RACS and VLASS2.1 observations (solid line) and with a spectral index of $\alpha_{\nu,\rm r} = 0.00 \pm 0.09$ derived from all radio measurements (dashed line).

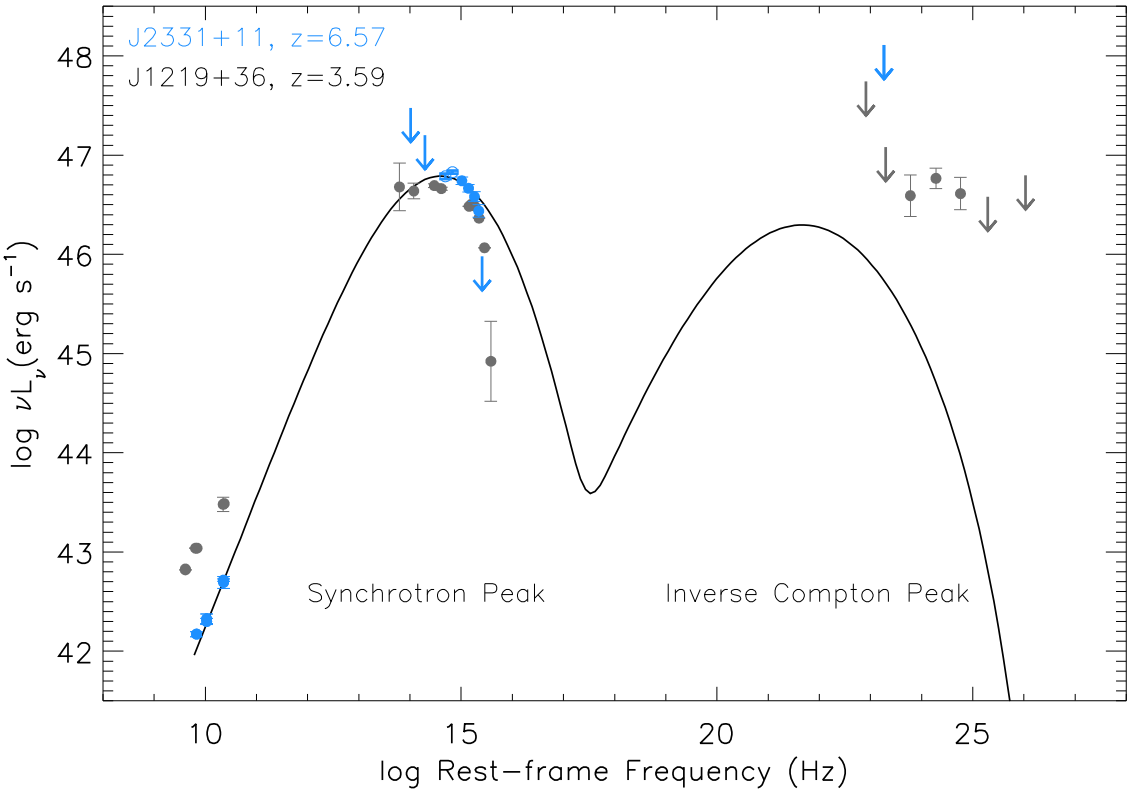

Extended Data Figure 4. SED and SED model of J2331+11. The observed SED of J2331+11 (blue symbols) is shown in comparison with the SED of the BL Lac object J1219+36 at $z = 3.59$[9] (dark grey symbols). The flux (luminosity) of the high-frequency side of the synchrotron peaks of J2331+11 and J1219+36 decreases quickly due to increasing absorption by neutral hydrogen in the intergalactic medium at high redshifts. The upper limit on the γ-ray luminosity of J2331+11 is estimated from the 10-year 5σ sensitivity map of the *Fermi Gamma-ray Space Telescope* Large Area Telescope (Fermi LAT) all-sky survey [48]. The black line shows the SSC emission model of the synchrotron and inverse Compton peaks of J2331+11.

References

1. Urry, C. M. & Padovani, P. Unified Schemes for Radio-Loud Active Galactic Nucle. *Publ. of the Astron. Soc. of the Pacific* **107**, 803-845 (1995)

2. Cavaliere, A. & D'Elia, V. The Blazar Main Sequence. *Astrophys. J.* **571**, 226-233 (2002)

3. Ajello, M. *et al.* The Cosmic Evolution of Fermi BL Lacertae Objects. *Astrophys. J.* **780**, 73 (2014)

4. Stickel, M., Padovani, P., Urry, C. M., Fried, J. W. & Kuehr, H. The Complete Sample of 1 Jansky BL Lacertae Objects. I. Summary Properties. *Astrophys. J.* **374**, 431 (1991)

5. O'Dowd, M., Urry, C. M. & Scarpa, R. The Host Galaxies of Radio-loud Active Galactic Nuclei: The Black Hole-Galaxy Connection. *Astrophys. J.* **580**, 96-103 (2002)

6. Best, P. N. *et al.* The host galaxies of radio-loud active galactic nuclei: mass dependences, gas cooling and active galactic nuclei feedback. *Mon. Not. R. Astron. Soc.* **362**, 25-40 (2005)

7. Shaw M. S. *et al.* Spectroscopy of the Largest Ever γ-Ray-selected BL Lac Sample. *Astrophys. J.* **764**, 135 (2013)

8. Massaro, E. *et al.* Roma-BZCAT: a multifrequency catalogue of blazars. *Astron. Astrophys.* **495**, 691-696 (2009)

9. Paliya, V. S. *et al.* The First Gamma-Ray Emitting BL Lacertae Object at the Cosmic Dawn. *Astrophys. J. Lett.* **903**, L8 (2020)

10. Dunlop, J. S. *et al.* Quasars, their host galaxies and their central black holes. *Mon. Not. R. Astron. Soc.* **340**, 1095 (2003)

11. McLure, R. J. & Jarvis, M. J. The relationship between radio luminosity and black hole mass in optically selected quasars. *Mon. Not. R. Astron. Soc.* **353**, L45-L49 (2004)

12. Ghisellini, G., Tavecchio, F., Maraschi, L., Celotti, A. & Sbarrato, T. The power of relativistic jets is larger than the luminosity of their accretion disks. *Nature* **515**, 376-378 (2014)

13. Paliya, V. S. *et al.* Blazars at the Cosmic Dawn. *Astrophys. J.* **897**, 177 (2020)

14. Ghisellini, G. *et al.* Chasing the heaviest black holes of jetted active galactic nuclei. *Mon. Not. R. Astron. Soc.* **405**, 387-400 (2010)

15. Ackermann, M. *et al.* Gamma-Ray Blazars within the First 2 Billion Years. *Astrophys. J. Lett.* **837**, L5 (2017)

16. Belladitta, S. *et al.* The first blazar observed at $z > 6$. *Astron. Astrophys. Lett.* **635**, L7 (2020)

17. Romani, R. W., Sowards-Emmerd, D., Greenhill, L., Michelson, P. Q0906+6930: The Highest Redshift Blazar. *Astrophys. J. Lett.* **610**, L9-L11 (2004)

18. Frey, S., Paragi, Z., Fogasy, J. O., & Gurvits, L. I. The first estimate of radio jet proper motion at $z > 5$. *Mon. Not. R. Astron. Soc.* **446**, 2921-2928 (2015)

19. Ghisellini, G., Haardt, F., Della Ceca, R., Volonteri, M., Sbarrato, T. The role of relativistic jets in the heaviest and most active supermassive black holes at high redshift. *Mon. Not. R. Astron. Soc.* **432**, 2818-2823 (2013)

20. Bañados, E. *et al.* The Discovery of a Highly Accreting, Radio-loud Quasar at $z = 6.82$. *Astrophys. J.* **909**, 80, (2021)

21. Abdo, A. A. *et al.* The Spectral Energy Distribution of Fermi Bright Blazars. *Astrophys. J.* **716**, 30-70 (2010)

22. Chiang, J. & Böttcher, M. Synchrotron and Synchrotron Self-Compton Spectral Signatures and Blazar Emission Models. *Astrophys. J.* **564**, 92-96 (2002)

23. Marscher, A. P. *et al.* The inner jet of an active galactic nucleus as revealed by a radio-to-γ-ray outburst. *Nature* **452**, 966-969 (2008)

24. Ghisellini, G., Tavecchio, F., Foschini, L. & Ghirlanda, G. The transition between BL Lac objects and flat spectrum radio quasars. *Mon. Not. R. Astron. Soc.* **414**, 2674-2689 (2011)

25. Marchã, M. J. M. & Caccianiga, A. The CLASS BL Lac sample: the radio luminosity function. *Mon. Not. R. Astron. Soc.* **430**, 2464-2475 (2013)

26. León-Tavares, J. *et al.* The connection between black hole mass and Doppler boosted emission in BL Lacertae type objects. *Mon. Not. R. Astron. Soc.* **411**, 1127-1136 (2011)

27. O'Dowd, M. & Urry, C. M. Host Galaxy Evolution in Radio-Loud Active Galactic Nuclei. *Astrophys. J.* **627**, 97-124 (2005)

28. Koptelova, E., Hwang, C.-Y., Malkan, M. A., Yu, P.-C. Host Galaxy Evolution in Rapidly accreting black hole of the Lyα-luminous quasar PSO J006.1240+39.2219. *Astrophys. J.* **882**, 144 (2019)

29. Gebhardt, K. *et al.* The Black Hole Mass in M87 from Gemini/NIFS Adaptive Optics Observations. *Astrophys. J.* **729**, 119 (2011)

30. Cole, S., Lacey, C. G., Baugh, C. M. & Frenk, C. S. Hierarchical galaxy formation. *Mon. Not. R. Astron. Soc.* **319**, 168-204 (2000)

31. Massaro, E. *et al.* The 5th edition of the Roma-BZCAT. A short presentation. *Astrophys. Space Science* **357**, 75 (2015)

32. Chambers, K. C. *et al.* The Pan-STARRS1 Surveys *eprint* arXiv:1612.05560 (2016)

33. White, R. L., Becker, R. H., Helfand, D. J., Gregg, M. D. A Catalog of 1.4 GHz Radio Sources from the FIRST Survey. *Astrophys. J.*, **475**, 479-493 (1997)

34. Helfand, D. J., White, R. L., Becker, R. H. The Last of FIRST: The Final Catalog and Source Identifications. *Astrophys. J.*, **801**, 26 (2015)

35. Lawrence, A. *et al.* The UKIRT Infrared Deep Sky Survey (UKIDSS). *Mon. Not. R. Astron. Soc.* **379**, 1599 (2007)

36. Hewett, P. C., Warren, S. J., Leggett, S. K., & Hodgkin, S. T. The UKIRT Infrared Deep Sky Survey ZY JHK photometric system: passbands and synthetic colours. *Mon. Not. R. Astron. Soc.* **367**, 454-468 (2006)

37. Schlafly, E. F., Meisner, A. M., Green, G. M. The unWISE Catalog: Two Billion Infrared Sources from Five Years of WISE Imaging. *Astrophys. J. Suppl.* **240**, 30 (2019)

38. Wright, E. L. *et al.* The Wide-field Infrared Survey Explorer (WISE): Mission Description and Initial On-orbit Performance. *Astron. J.*, **140**, 1868 (2010)

39. Mainzer, A. *et al.* Preliminary Results from NEOWISE: An Enhancement to the Wide-field Infrared Survey Explorer for Solar System Science. *Astrophys. J.* **731**, 53 (2011)

40. McConnell, D. *et al.* The Rapid ASKAP Continuum Survey I: Design and first results. *Publ. of the Astron. Soc. of Australia* **37**, e048, (2020)

41. Lacy, M. *et al.* The Karl G. Jansky Very Large Array Sky Survey (VLASS). Science Case and Survey Design. *Publ. of the Astron. Society of the Pacific* **132**, 035001, (2020)

42. Condon, J. J. *et al.* The NRAO VLA Sky Survey. *Astron. J.* **115**, 1693-1716, (1998)

43. Elias, J. H. *et al.* Design of the Gemini near-infrared spectrograph. *Proc. SPIE* **6269**, 62694C, (2006)

44. Konigl, A. Relativistic jets as X-ray and gamma-ray sources. *Astrophys. J.* **243**, 700-709 (1981)

45. Massaro, E., Tramacere, A., Perri, M., Giommi, P., & Tosti, G. Log-parabolic spectra and particle acceleration in blazars. III. SSC emission in the TeV band from Mkn501. *Astron. Astrophys.* **448**, 861-871 (2006)

46. Tramacere, A., Giommi, P., Perri, M., Verrecchia, F., & Tosti, G. Swift observations of the very intense flaring activity of Mrk 421 during 2006. I. Phenomenological picture of electron acceleration and predictions for MeV/GeV emission. *Astron. Astrophys.* **501**, 879-898 (2009)

47. Abdo, A. A. *et al.* Fermi Large Area Telescope Observations of Markarian 421: The Missing Piece of its Spectral Energy Distribution. *Astrophys. J.* **736**, 131 (2011)

48. Atwood, W. B. *et al.* The Large Area Telescope on the Fermi Gamma-Ray Space Telescope Mission. *Astrophys. J.* **697**, 1071-1102 (2009)

Acknowledgements Based on observations obtained at the international Gemini Observatory (Program ID: GN-2020B-FT-109) which is managed by the Association of Universities for Research in Astronomy (AURA) under a cooperative agreement with the National Science Foundation on behalf of the Gemini Observatory partnership: the National Science Foundation (United States), National Research Council (Canada), Agencia Nacional de Investigación y Desarrollo (Chile), Ministerio de Ciencia, Tecnología e Innovación (Argentina), Ministério da Ciência, Tecnologia, Inovações e Comunicações (Brazil), and Korea Astronomy and Space Science Institute (Republic of Korea).
Based on observations obtained with UKIRT (Program ID: U/20B/NCU02). UKIRT is owned by the University of Hawaii (UH) and operated by the UH Institute for Astronomy; operations are enabled through the cooperation of the East Asian Observatory.

Author contributions E.K. selected the source, conducted the observations and data analysis. C.-Y. H. conducted the observations and data analysis.

Data availability The spectroscopic data presented in the paper are available from the Gemini Observatory Archive. The paper also used the catalogues and images available online.

Code availability The spectra were analysed using the Gemini IRAF package available from the Gemini

403 webpage. The SED model was calculated using the web-based numerical SSC code.

404

405 **Correspondence** Correspondence and requests for materials should be addressed to E.K. and C.-Y. H. (emails:

406 koptelova@astro.ncu.edu.tw, hwangcy@astro.ncu.edu.tw).

407 **Competing Interests** The authors declare that they have no competing financial interests.

Extended Data Table 1. Photometry of J2331+11.

Telescope/ Instrument	Obs. Date (yy-mm-dd)	MJD	Filter	$\lambda_{\rm eff}$ Å	$m_{\rm AB}$
PS1	$2011-2014$		$z_{\rm PS1}$	8667	>22.30 (5σ)
PS1	$2011-2014$		$y_{\rm PS1}$	9613	21.195±0.169
UKIRT/WFCAM	$2009-09-03$	55077.37985	Y	10305	21.803±0.522
UKIRT/WFCAM	$2009-09-03$	55077.39387	J	12483	21.150±0.302
UKIRT/WFCAM	$2009-11-03$	55138.32198	H	16313	19.995±0.154
UKIRT/WFCAM	$2009-11-03$	55138.33587	K	22010	19.907±0.130
UKIRT/WFCAM	$2020-11-03$	59156.33387	Z	8817	>22.95 (5σ)
UKIRT/WFCAM	$2020-11-03$	59156.34357	Y	10305	21.637±0.157
UKIRT/WFCAM	$2020-11-03$	59156.35104	J	12483	21.067±0.123
UKIRT/WFCAM	$2020-11-03$	59156.35519	H	16313	20.569±0.095
UKIRT/WFCAM	$2020-11-03$	59156.35808	K	22010	20.053±0.092
WISE	$2010-2017$		$W1$	33526	19.380±0.039
WISE	$2010-2017$		$W2$	46028	19.138±0.068
WISE	$2010-2011$		$W3$	115608	>17.07 (2σ)
WISE	$2010-2011$		$W4$	220883	>15.64 (2σ)

Notes. Survey and Instrument name (Col. 1), date of observations (Col. 2), Modified Julian Day (MJD) of observations (Col. 3), filter name (Col. 4), effective wavelength of the filter $\lambda_{\rm eff}$ (Col.

410 5), and AB magnitude and magnitude uncertainty (Col. 6).

Extended Data Table 2. Integrated radio flux densities of J2331+11.

Survey name	Obs. date (yy-mm-dd)	$\nu_{\rm obs}$ (GHz)	$f_\nu^{\rm obs}$ (mJy)	$\sigma_{f_\nu^{\rm obs}}$ (mJy)
RACS	2020-11-02	0.888	2.50	0.07
NVSS	1996-07-04	1.4	2.26	0.34
FIRST	2011-03-19	1.4	2.13	0.15
VLASS1.1	2017-10-25	3.0	2.59	0.25
VLASS2.1	2020-08-29	3.0	2.46	0.15

411 **Notes.** Survey name (Col. 1), epoch of observations (Col. 2), observed frequency $\nu_{\rm obs}$ (Col. 3),
412 observed integrated flux density $f_\nu^{\rm obs}$ (Col. 4), and flux density uncertainty $\sigma_{f_\nu^{\rm obs}}$ (Col. 5).

Extended Data Table 3. Parameters of the synchrotron SSC emission model.

Parameter	Value
$t_{\rm var}$ (s)	5.27×10^6
R (cm)	2.1×10^{16}
B (G)	0.4
N (cm^{-3})	10
δ	31.5
$\gamma_{\rm peak}$	10^3
$\gamma_{\rm min}$	10^{-1}
$\gamma_{\rm max}$	10^6
r	2.2
$\nu^{\rm S}_{\rm peak}$ (Hz)	3.4×10^{14}
$L_{\rm S}$ (erg s^{-1})	2.4×10^{47}

Notes. $t_{\rm var}$ is the variability timescale, R is the radius of the emitting region constrained by $t_{\rm var}$, δ is the Doppler factor, B is the intensity of the magnetic field, N is the electron density, $\gamma_{\rm peak}$ is the electron Lorentz factor at the peak of the electron energy distribution, $\gamma_{\rm min}$ and $\gamma_{\rm max}$ are the minimum and maximum Lorentz factors of the electron energy distribution, r is the curvature parameter of the electron energy distribution, $\nu^{\rm S}_{\rm peak}$ is the rest-frame peak frequency of the synchrotron peak, and $L_{\rm S}$ is the total luminosity of the synchrotron peak.